

# Shape Conformal and Thermal Insulative Organic Solar Absorber Sponge for Photothermal Water Evaporation and Thermoelectric Power Generation

Liangliang Zhu, Tianpeng Ding, Minmin Gao, Connor Kang Nuo Peh, and Ghim Wei Ho\*

Solar-driven interfacial vaporization by localizing solar-thermal energy conversion to the air–water interface has attracted tremendous attention due to its high conversion efficiency for water purification, desalination, energy generation, etc. However, ineffective integration of hybrid solar thermal devices and poor material compliance undermine extensive solar energy exploitation and practical outdoor use. Herein, a 3D organic bucky sponge that has a combination of desired chemical and physical properties, i.e., broadband light absorbing, heat insulative, and shape-conforming abilities that render efficient photothermic vaporization and energy generation with improved operational durability is reported. The highly compressible and readily reconfigurable solar absorber sponge not only places less constraints on footprint and shape defined fabrication process but more importantly remarkably improves the solar-to-vapor conversion efficiency. Notably, synergetic coupling of solar-steam and solar-electricity technologies is realized without trade-offs, highlighting the practical consideration toward more impactful solar heat exploitation. Such solar distillation and low-grade heat-to-electricity generation functions can provide potential opportunities for fresh water and electricity supply in off-grid or remote areas.

Solar energy is an inexhaustible energy source for the development of sustainable energy technology. Solar-to-thermal technology is a direct strategy for harvesting solar energy, which

Dr. L. L. Zhu, Dr. T. P. Ding, Dr. M. M. Gao, Dr. C. K. N. Peh, Prof. G. W. Ho  
Department of Electrical and Computer Engineering  
National University of Singapore  
4 Engineering Drive 3, 117583 Singapore, Singapore  
E-mail: elehgw@nus.edu.sg

Dr. L. L. Zhu  
State Key Laboratory of Materials-Oriented Chemical Engineering  
College of Chemical Engineering  
Nanjing Tech University  
No. 30 South Puzhu Road, Nanjing 211816, P. R. China

Prof. G. W. Ho  
Engineering Science Programme  
National University of Singapore  
9 Engineering Drive 1, 117575 Singapore, Singapore

Prof. G. W. Ho  
Institute of Materials Research and Engineering  
A\*STAR Agency for Science, Technology and Research  
3 Research Link, 117602 Singapore, Singapore

 The ORCID identification number(s) for the author(s) of this article can be found under <https://doi.org/10.1002/aenm.201900250>.

DOI: 10.1002/aenm.201900250

can attain the highest achievable conversion efficiency and enable a broad range of applications, including domestic heating, brine desalination, wastewater purification, steam sterilization, and power generation.<sup>[1–7]</sup> One actualization of solar-to-thermal technology, solar-driven water evaporation can directly transfer heat to drive evaporation using sunlight as the only power input.<sup>[8–15]</sup> Compared with the conventional solar-driven steam generation system which requires high optical devices and large footprints investment, the emerging interfacial photothermal water evaporation based on nanostructured solar receiver materials restrict the solar heat at the water–air interface to suppress the heat losses and enhance the conversion efficiency. To date, significant progress in preparation of solar absorber materials, including semiconductors,<sup>[16–18]</sup> metallic,<sup>[19–21]</sup> and carbonaceous nanomaterials,<sup>[22–25]</sup> alongside with prudent system designs, e.g., environmental enhancement,<sup>[26–28]</sup> optical,<sup>[28–30]</sup> and thermal management<sup>[31–33]</sup> have been made to improve solar energy conversion efficiency. However, extended and collaborative utilization of nonconcentrated solar energy conversion for practical applications is making a little headway due to inconsequential/conflicting outcomes. On one hand, the heat losses from the solar absorber to bulk water and surrounding air for water vaporization are inevitable. On the other hand, constructive low-grade solar heat harvesting during evaporation are rarely reported. Therefore, effective thermal management and synergic utilization of the solar steam generation are essential. Another major roadblock toward photothermal technological advancement is the accessibility to a robust and practical material structure for practical deployment. As such, lightweight, load bearing, weather resistant, and uncommonly shape adaptive solar absorber materials are long sought after for durable outdoor application.

Herein, we report a 3D organic bucky sponge that is collectively elastic, broadband light absorbing, and heat insulative that enables desired combination of efficient solar thermal conversion and mechanical stability. The 3D cellular truss is highly compressible and elastic which assumes excellent shape conformity and recovery, particularly beneficial to maximize space usage as well as for flexible, resilient outdoor purposes. Importantly, a rational integration of efficient solar water

evaporation and waste solar heat harvesting for thermoelectric (TE) power generation under practical 1 sun is demonstrated. The use of solar absorber sponge has mutually addressed the superfluous heat losses, space/structural constrains, and performance metrics by enabling hybrid solar thermal technologies in a collaborative fashion. Such complementary photothermal evaporation and generator highlights the seamless integration of low grade waste heat technologies, envisioned for practical outdoor solar distillation and electricity generation applications.

The sponge is prepared by solution coating of carbon nanotubes/cellulose nanocrystals (CNT/CNC) nanocomposite on a polydimethylsiloxane (PDMS) sponge, refer as a PCC sponge. The resultant PCC sponge possesses a favorable inbuilt structural hierarchy with elastic macroporous open cells, which are ideal scaffolds for water wicking and holding.<sup>[25,34]</sup> The broadband light absorber CNT/CNC nanocomposites essentially contributes to efficient solar steam generation. Moreover, taking advantage of superior compressibility of PDMS, the shape adaptiveness of PCC sponge can conform/comply to any arbitrary shaped medium or surroundings, thereby saving space and improving efficiency. Notably, the open cell structure allows the sponge to be directly used as a freestanding water reservoir, endowed with capillary liquid wicking within the sponge to the hot spot. By doing so, the solar absorber is purposely isolated from the bulk water body, eliminating the heat losses to bulk water and significantly boosting in situ photothermal vaporization. More importantly, by rational engineering design, a demonstration of efficient solar water evaporation and complementary solar heating to sustain electricity generation under practical 1 sun is presented (Figure 1). Temperature difference between PCC sponge and bulk water occurs during the solar evaporation because of the heat localization effect. Hence, a TE module which is triggered by static temperature differences via the Seebeck effect was used to harvest this low-grade solar heat for waste energy-to-electricity conversion.<sup>[35]</sup> Meanwhile, the TE module serves as a thermal insulator under PCC sponge to promote the solar evaporation. This approach provides a new opportunity for generating fresh water and electricity on-demand/on-site which is especially attractive for off-grid areas.

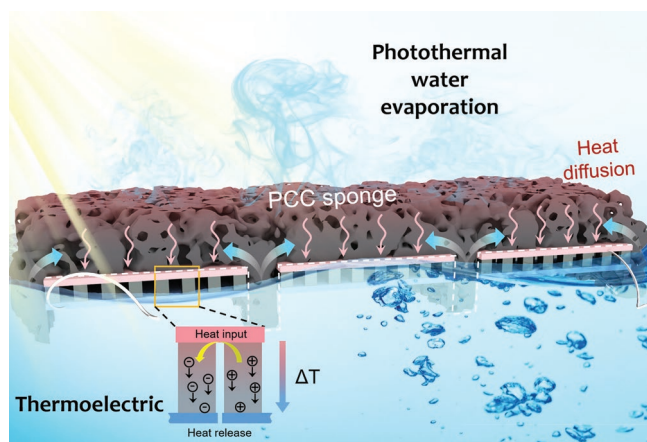


**Figure 1.** Schematic of the synergistic interfacial photothermal water evaporation and thermoelectricity generation process based on PCC sponge.

Figure 2a shows the synthesis strategy for preparing the 3D porous PCC sponge. A homogeneous PDMS gel precursor containing silicone elastomer/curing agents was first mixed.<sup>[36–39]</sup> Sugar cube (Figure S1a,b, Supporting Information) were used as sacrificial PDMS template to produce 3D porous PDMS sponges. The as-prepared PDMS sponge has an interconnected network architecture and in-built rough surface (Figure 2b and Figure S1c,d, Supporting Information), which provides an ideal structure for immobilization of photothermal nanomaterials and water wicking pathway. Due to its low density ( $0.16 \pm 0.01 \text{ g cm}^{-3}$ , Equation (S1), Supporting Information), the PDMS sponge stays afloat on water, as shown in Figure S2 (Supporting Information). The CNT nanocomposite constructed by cross-linked CNTs and CNCs is employed to provide solar absorption and solar thermal conversion functionalities (Figure S3, Supporting Information). Scanning electron microscopy (SEM) images in Figure 2c and Figure S4 (Supporting Information) reveal that the PCC sponge has a similar 3D interconnected network architecture to that of PDMS sponge, however, with an additional uniform coating of the CNT/CNC nanocomposites. The corresponding digital photos of PDMS and PCC sponges are shown in Figure 2b,c (insets), displaying the sponge color changes from white to black. Likewise, PCC sponge also possesses high elasticity and low density characteristics, resulting in a complete recovery after sustaining a large compression deformation (Figure 2d and Figure S5, Supporting Information) and free floating at the water–air interface (Figure 2e), respectively. Moreover, the PCC sponge (with a thickness of 5 mm) exhibits extremely small optical transmittance ( $<0.1\%$ ) and reflectance ( $\approx 3\text{--}7\%$ ) in the visible and near infrared spectra, suggesting the prominent light absorptance of the PCC sponge (Figure 2f). The remarkable absorptance owes to the optical absorption of the CNT/CNC absorber and the light scattering from the inbuilt hierarchical structures that increase the optical path length within the PCC sponge. As a result, the PCC sponge can easily reach more than  $82 \text{ }^\circ\text{C}$  in 2 min under 1 sun (Figure 2g), in contrast to the PDMS sponge which only attains  $31 \text{ }^\circ\text{C}$  (Figure S6, Supporting Information). The excellent light absorbance characteristic of the sponge structure along with the superior photothermal conversion of CNT/CNC makes the PCC sponge a desirable candidate for solar vaporization.

In addition, the 3D porous structure in PCC sponge plays a thermal insulator role due to the low thermal conductivity of PDMS.<sup>[40,41]</sup> Compared with CNT/CNC membrane (CNT/CNC dispersion coated on hydrophilic mixed cellulose ester filter membrane) (Figure S7a, Supporting Information), PCC sponge shows a faster temperature increase under the light irradiation but a slower decrease in dark. As shown in Figure 3a, PCC sponge takes  $\approx 120 \text{ s}$  to heat up to  $60 \text{ }^\circ\text{C}$ , which is about 60 s quicker than that of CNT/CNC membrane. When the simulated sunlight is switched off, PCC sponge takes nearly twice as long for cooling to the room temperature than the CNT/CNC membrane. Furthermore, interfacial water heating is enabled under light irradiation as experimentally verified in the temperature-distance plots (Figure 3b and Figure S8, Supporting Information). Clearly, the PCC sponge exhibits a localized sharp peak in the temperature profile, while a smooth water temperature profile in the absence of PCC sponge suggests bulk water heating. The decreasing shoulder appeared after the sharp peak

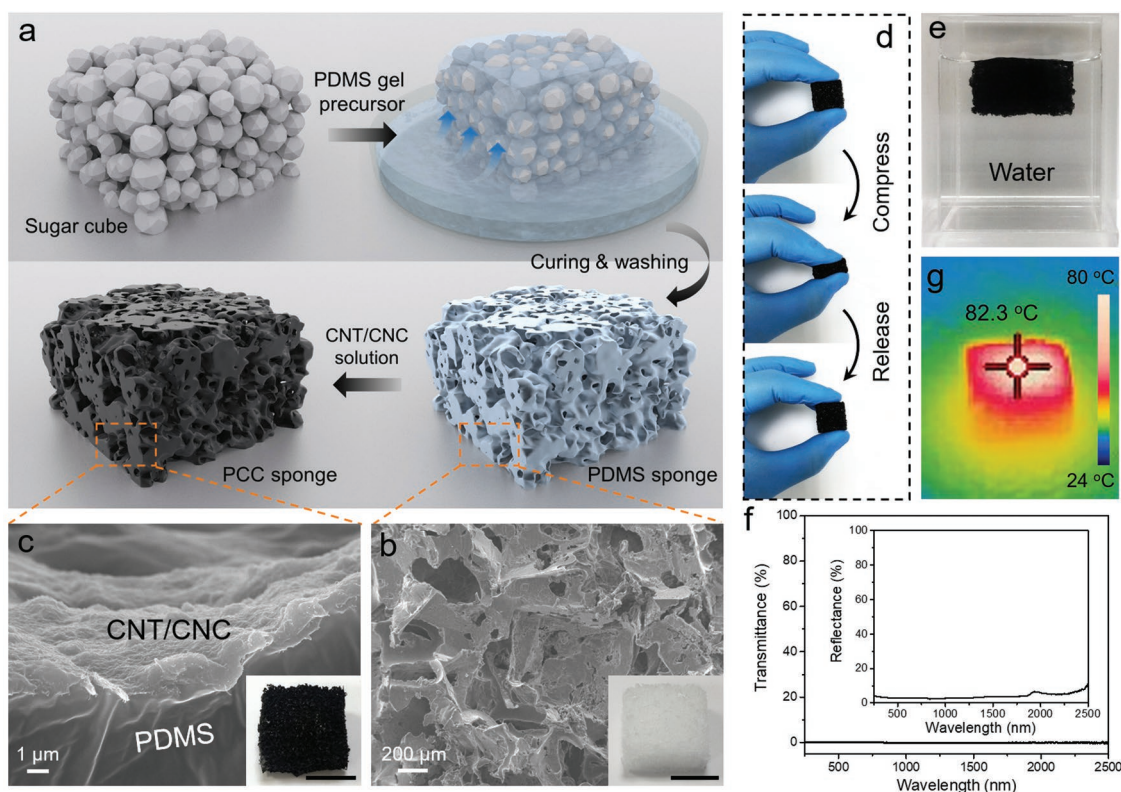


**Figure 2.** a) Schematic of preparation procedures of PCC sponge. SEM images of PDMS b) and PCC c) sponge; insets: digital photographs of PDMS b) and PCC c) sponge, inset scale bar is 1 cm. d) Photographs of the PCC sponge under a compressing and releasing cycle. e) Photograph of a block of CS25 floating on the water. f) Transmittance and reflectance spectra of PCC sponge. g) Infrared image of PCC sponge under 1 sun for 2 min.

is attributed to the higher temperature of side of PCC sponge, suggesting the trapping of photothermal heat.

The outstanding light absorption and thermal management of PCC sponge provide a unique opportunity for highly efficient photothermal evaporation systems. Therefore, interfacial solar-driven water evaporation using the PCC sponges was demonstrated (Figure 3c). Under solar irradiation, the PCC sponge can float at the air/water interface, efficiently heat up interfacial region, and generate steady steam flux. The PCC sponges loaded with different CNT/CNC amount (based on the CNT/CNC dispersion concentrations: 0.02, 0.2, 1, and 2 mg mL<sup>-1</sup>) were prepared and applied in solar steam generation, which are referred to as PCC<sub>0.02</sub>, PCC<sub>0.2</sub>, PCC<sub>1</sub>, and PCC<sub>2</sub> sponges, respectively (Figure S9, Supporting Information). The evaporation rate of the PCC sponge was quantified by recording the weight loss of water over time (Figure 2d). The rates of the evaporation for blank, PCC<sub>0.02</sub>, PCC<sub>0.2</sub>, PCC<sub>1</sub>, and PCC<sub>2</sub> sponges are 0.32, 1.06, 1.22, 1.35, and 1.35 kg m<sup>-2</sup> h<sup>-1</sup> after 1 h evaporation stabilization. The corresponding conversion efficiencies ( $\eta$ ) are calculated to be 19.1%, 68.2%, 78.5%, 87.4%, and 87.4%, respectively (Equations (S2) and (S3), Supporting Information). In contrast, membrane evaporator shows an evaporation rate of 0.85 kg m<sup>-2</sup> h<sup>-1</sup> under the same condition (Figure S7b, Supporting Information). It is apparent that PCC sponge with 3D porous structure significantly enhances the light-to-steam efficiency, which is comparable with other similar 3D structures (Table S1, Supporting Information). Among the different CNT/CNC loadings, the PCC<sub>1</sub> sponge shows a similar

evaporation rate and efficiency as the PCC<sub>2</sub> sponge, indicating the optimized loading amount is 1 mg mL<sup>-1</sup> CNT/CNC dispersion. Moreover, the surface temperature of PCC<sub>1</sub> sponge is  $\approx$ 43.7 °C which is  $\approx$ 10.9 °C higher than that of water without PCC sponge (Figure 3e). The results reveal heat localization at the evaporative PCC sponge surface so as to minimize heat loss and augment photothermal conversion efficiency. Furthermore, the evaporation measurement was also carried out for 8 h and the result shows no obvious deterioration of water evaporation ability, suggesting the PCC sponge is highly stable and robust for long-term use (Figure S10, Supporting Information).

Owing to its high elasticity, PCC sponge can be easily adapted into different molds to intentionally adjust the density of sponge, which potentially allows maximal utilization of evaporation on-site space (Figure 4a,b). Specifically, prefabricated acrylic molds of various shapes, e.g., square, parallelogram, circle, and curved square, are employed as evaporator media, as shown in Figure S11 (Supporting Information). The same piece of PCC sponge of size of 17 mm  $\times$  17 mm can readily configure into the different size molds, and the effective evaporation areas are calculated to be 2.89,  $\approx$ 2.5,  $\approx$ 2.27, and  $\approx$ 1.94 cm<sup>2</sup>, respectively. The obtained evaporation rates of the compressed sponges (parallelogram, circle, and curved square) increase to 105.5%, 108.3%, and 110.9% as compared to uncompressed sponge (square) due to their denser fibrils network (Figure 4c). The PCC sponge also shows its perfect shape recovery attribute after its removal from the molds, indicating the mechanical stability and robustness for recycling and reconfiguration

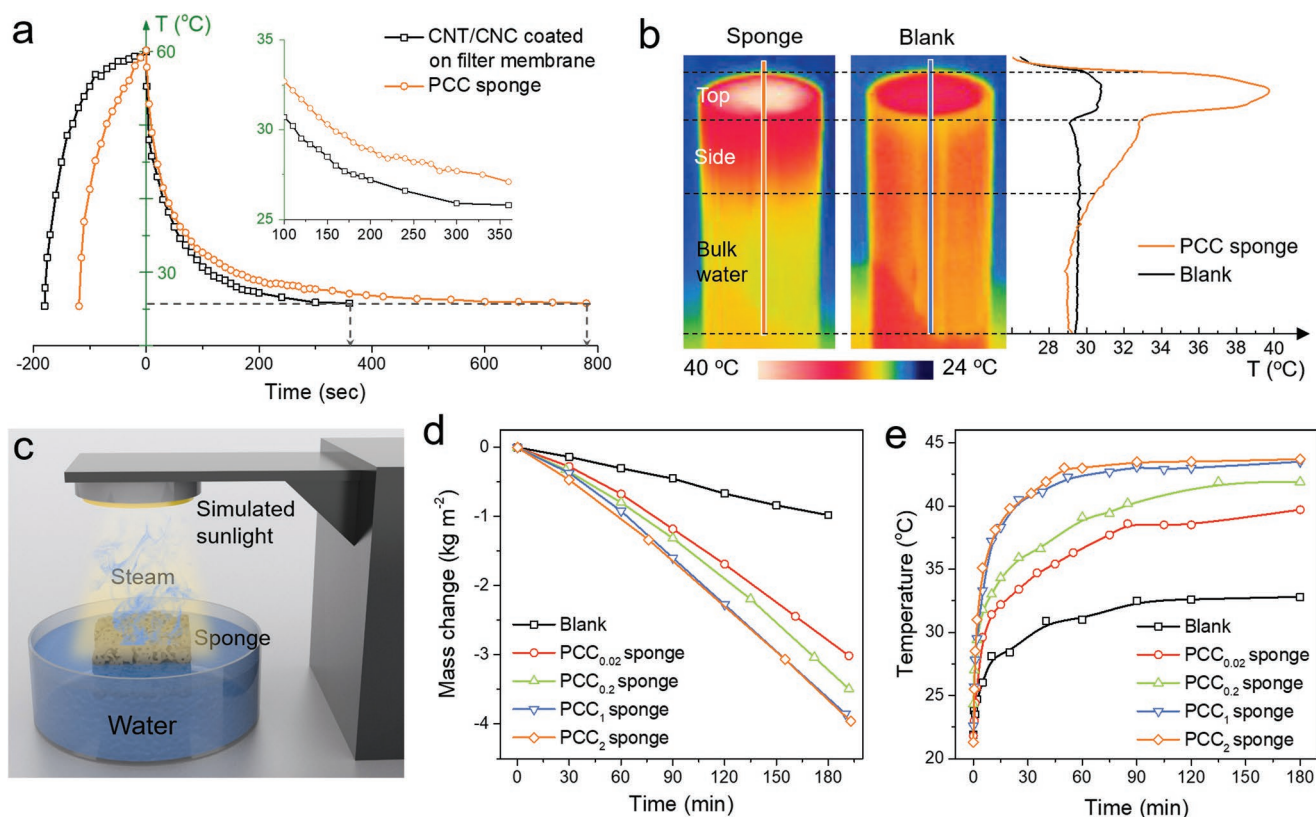


**Figure 3.** a) Temperature changes of CNT/CNC membrane and PCC sponge at an optical density of  $1 \text{ kW m}^{-2}$ . b) Temperature profiles of water–air interface with and without PCC sponge under light irradiation for 30 min at an optical density of  $1 \text{ kW m}^{-2}$ . c) The schematic illustration of solar steam generation. The mass changes d) and corresponding surface temperature changes e) of different PCC sponges over time at an optical density of  $1 \text{ kW m}^{-2}$ .

(Figure S12, Supporting Information). Additionally, PCC sponge can fit in other molds with much more complicated shapes (divergent lines and concentric circles), displaying its great shape adaptiveness and conformity properties (Figure 4b). Furthermore, based on the elastic and water holding abilities of the cellular sponge, self-containing mode which directly employs the sponge as a freestanding water reservoir and a light absorber is also examined.<sup>[25,34]</sup> The PCC sponge wicks and confines water within its hierarchical cellular pores to perform in situ photothermal evaporation (Figure 4d). A truly heat localization is achieved owing to the evaporation system is thermally isolated from the surrounding water. Thus, the bulk water heat losses are largely eliminated and consequentially enhance the photothermic vaporization efficiency. The steam generation rate increases up to 112.6% in the first 3 h as compared to the contact mode, after which the evaporation rate obviously decreases due to the excessive reduction of water contained in the PCC sponge (Figure 4c (orange),e). Importantly, the PCC sponge is able to regain its high vaporization rate upon the water replenishment (Figure 4e). The surface temperature of PCC sponge is monitored by IR camera, showing  $\approx 42 \text{ }^\circ\text{C}$  during the stable evaporation process and more than  $55 \text{ }^\circ\text{C}$  at the edge of sponge after 3 h of evaporation due to the reduction of water containing in the sponge (Figure 4f). All these findings explicitly demonstrate the enhanced localized interfacial heating capable of offering an energy- and cost-efficient approach for solar-driven water evaporation.

Due to the heating localization, the surface temperature of the PCC sponge is higher than that in bulk water during the solar evaporation. This low-grade solar heat is perceived as a promising energy source for waste energy-to-electricity conversion.<sup>[35]</sup> We used a TE module to harvest the low-grade heat via the Seebeck effect triggered by static temperature differences between the solar absorber and bulk water (Figure 5a,b).<sup>[42–44]</sup> The PCC sponges are readily shaped to conformally cover the upper side of TE module with a wall contacting with bulk water for efficient water transportation (Figure 5b). With the assistance of a polystyrene (PS) foam frame, the lower side of the TE module is just immersed into bulk water, as shown in Figure 5c. To do this, the upper side gains a higher temperature from the photothermal heat diffusion of PCC sponge, while the lower side is cooled by the bulk water, resulting in an effective temperature difference. Moreover, TE module herein also serves as a thermal insulator to isolate the PCC sponge from bulk water, which could improve the water evaporation rate. A PCC sponge with a thickness of 2 mm is used in water evaporation with and without TE module underneath (Figure S13, Supporting Information). The evaporation rates are measured to be 1.36 and  $1.20 \text{ kg m}^{-2} \text{ h}^{-1}$ , respectively, indicating the reduction of heat loss by the thermal insulation of TE module (Figure 5d). The thermoelectric effect is measured via a commercial TE module (TEP1-097T200, waterproof) during the evaporation transition (Figures S14–S16, Supporting Information). The temperature differences and the electrical signal outputs of TE module are

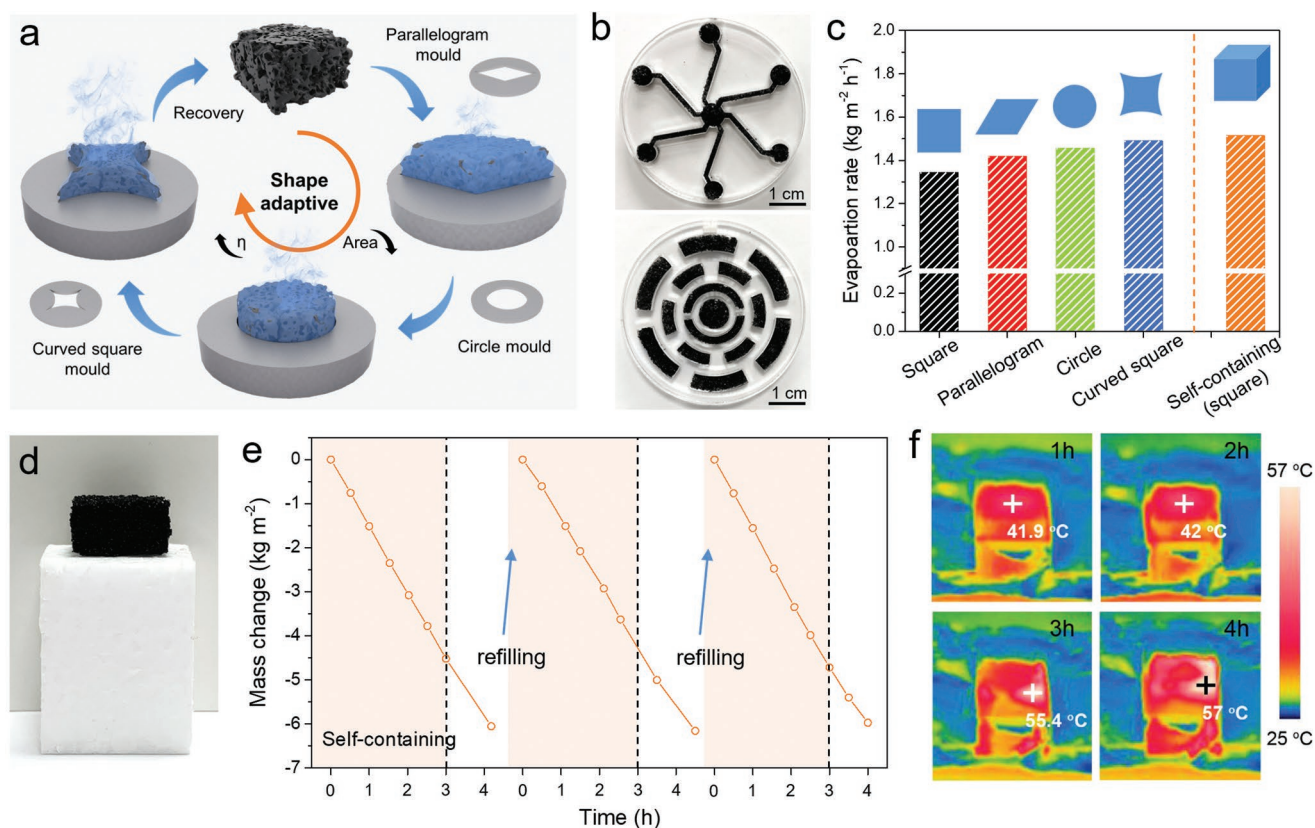


**Figure 4.** a) Schematic of shape adaptive property of PCC sponge. b) Photographs of PCC sponge adapted in different molds. c) The evaporation rates of the PCC sponge adapted in different molds and self-containing configuration at an optical density of 1 kW m<sup>-2</sup>. d) Photograph of PCC sponge contained water in air. e) The evaporation mass loss in containing configuration at an optical density of 1 kW m<sup>-2</sup>. f) The infrared images of PCC sponge during the evaporation in containing configuration.

recorded in Figure 5e,f. The obtained maximum open circuit voltages ( $V_{oc}$ ) are  $\approx 60$ , 110, and 263 mV (Figure 5f), which are resulted from the temperature differences of  $\approx 4.6$ , 8.3, and 14.8 °C, respectively, from the photothermal heating at optical densities of 1, 2, and 5 kW m<sup>-2</sup> (Figure 5e and Figure S17, Supporting Information). In contrast, a much lower thermoelectric voltage of  $\approx 26$  mV is attained in the absence of PCC sponge under 1 sun (2 °C difference in temperature), revealing the synergistic enhancement of water evaporation and thermoelectric energy generation. The corresponding short circuit current ( $I_{sc}$ ) are 26, 47, and 110 mA under 1, 2, and 5 sun (Figure S18, Supporting Information). The output voltage, current, and power were measured using an external loading resistance (Figures S19–S22, Supporting Information). As the loading resistance increases, the output voltage increases, while the output current decreases under the different light intensities. The calculated output power ascends then descends with the increasing loading resistance. The maximum output power was achieved when external resistance is about 2  $\Omega$  and output power is 0.05, 0.32, 0.87, and 5.38 mW without and with PCC sponge under 1, 2, and 5 sun, respectively (Figure 5g), with corresponding output power density of and 0.063, 0.4, 1.09, and 6.73 W m<sup>-2</sup>, respectively. To generate practically useful levels of power, four modular units of photothermal steam and thermoelectric generator are assembled, while leaving gaps between each module (Figure S23a, Supporting Information).

The PCC sponges can easily be conformed to fit the gaps and cover the TE surface due to its highly elasticity and shape adaptiveness, facilitating unobstructed water transport to the surface (Figure S23b,c, Supporting Information), and appreciable photothermal steam generation. Under the simulated sunlight, the generated thermoelectric power proportionally increases. Under 5 sun, an electronic calculator can be powered (Figure 5g (inset) and Figure S23a, Supporting Information). It should also be noted that two or more units can be connected in series on-site/on-demand, suggesting feasible large-scale integrated solar thermal applications (Figure S23b, Supporting Information). Figure 5h shows  $V-t$  curves acquired with three light on/off cycles, displaying an obvious photosensitivity, which verifies a photothermal-induced thermoelectric generation.

However, the electrical potentials decrease over the time, particularly evident in the higher solar irradiation intensity (Figure 5f,h), which is attributed to the inevitable temperature increase of limited static bulk water that we used in the experiments (600 mL) under the continuous light irradiation (Figure S17b, Supporting Information and Figure 5e,i (upper)). Evidently, similar trend of temperature difference and voltage change can be observed in Figure 5e,f. Nevertheless, the natural water bodies, e.g., lakes, seas, and oceans, can be regarded as unlimited waters and their temperature remain consistent over time. Based on the typical average temperature of sea water around the big cities (Figure S25, Supporting Information),

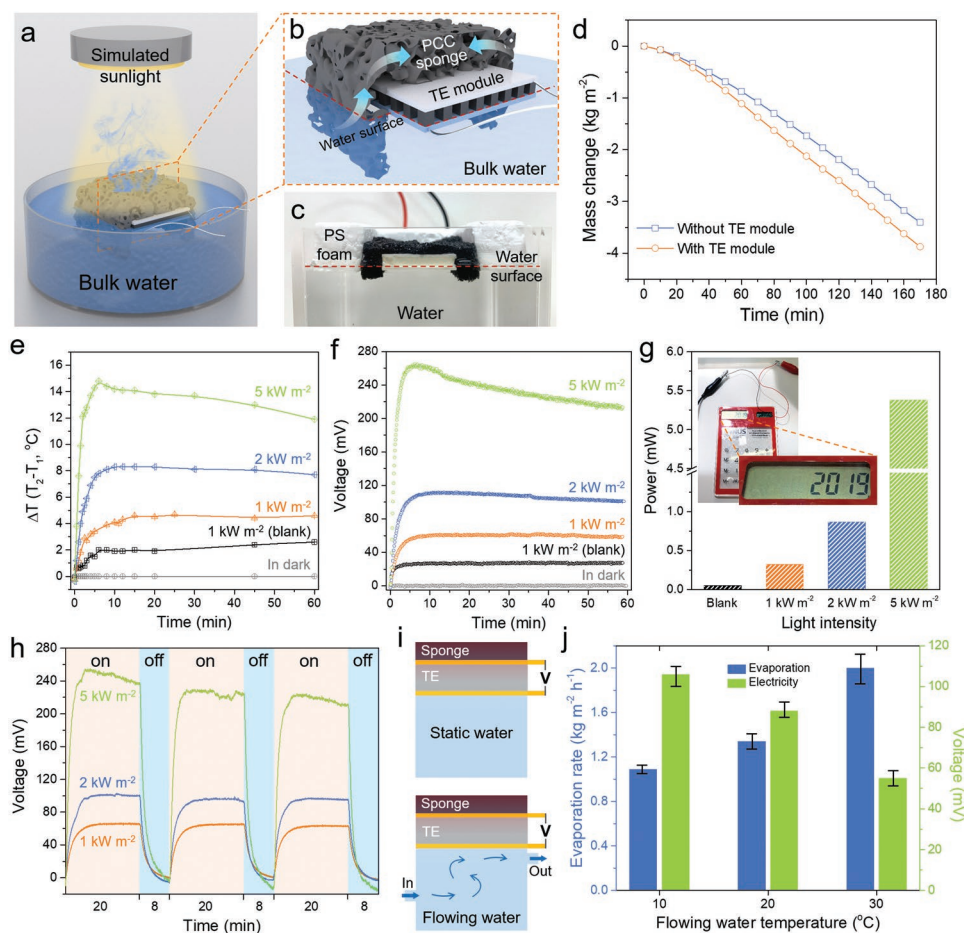


**Figure 5.** a) Schematic of simultaneous generations of electricity and steam. b) Schematic and c) photograph of electricity and steam generation device. d) The evaporation mass loss of PCC sponge with and without TE module at an optical density of  $1 \text{ kW m}^{-2}$ . e) Temperature difference between sides of TE module and f) the corresponding open circuit voltage under the different solar irradiances. g) Maximum output power of the TE device under different solar irradiances. h) Light response of the TE device under different solar irradiances. i) Schematic of thermoelectric power generation under static and flow bulk water. j) The water evaporation rate and open circuit voltage of TE module at flowing water temperature of 10, 20, and 30 °C under an optical density of  $1 \text{ kW m}^{-2}$ .

water bath of 30, 20, and 10 °C is circulated to simulate the natural sea water condition (Figure 5i, lower). It can be seen that the water evaporation rate decreases as the flowing water temperature decreases under 1 sun, namely, 2.01, 1.33, and  $1.09 \text{ kg m}^{-2} \text{ h}^{-1}$ , respectively (Figure 5j, blue). However, the lower temperature of bulk water leads to a larger temperature difference, resulting in a higher thermoelectric potential. As shown in Figure 5j (green), the voltages reach up to 106, 88, and 55 mV for flowing water temperature of 10, 20, and 30 °C under 1 sun (Figure S26, Supporting Information). Collectively, the as-designed photothermal evaporation and thermoelectricity generation device based on PCC sponge is a synergic strategy for clean water and energy generation, improving the overall comprehensive solar utilization.

In summary, we have demonstrated a highly compressible and easily reconfigurable all organic solar absorber sponge for hybrid photothermal technologies. The PCC sponge possesses a broadband optical absorption and favorable inbuilt structural hierarchy to form elastic macroporous open cells, which are desirable for high photothermal conversion, efficient

fluid capillarity, and effective heat insulation. The evaporation efficiency achieved under 1 sun is 87.4%, which can be greatly enhanced by compressing the sponge to densify the fibrils network or to operate under self-containing evaporation mode to eliminate the heat losses to bulk water. The integral design of simultaneous generation of clean water and electricity are also demonstrated. Thermoelectric module serves as heat insulator for improving solar water evaporation and synchronously harvests low-grade solar heat to sustain electricity under practical 1 sun. The use of all-inclusive compressible, light absorbing, and thermal insulative material overcome shape/structural rigidity and redundant heat losses toward promising solar energy based decentralized water and electricity generation technology for remote rural areas.

## Supporting Information

Supporting Information is available from the Wiley Online Library or from the author.

## Acknowledgements

This work was supported by the Ministry of Education (MOE) under Grant Nos. R-263-000-D18-112 and R-263-000-C85-112 and Singapore Ministry of National Development and the National Research Foundation, Prime Minister's Office under the Land and Liveability National Innovation Challenge (L2 NIC) Research Programme (L2 NIC Award No. L2NICCFP2-2015-3).

## Conflict of Interest

The authors declare no conflict of interest.

## Keywords

electricity generation, interfacial solar steam generation, PDMS sponge, photothermic vaporization, thermoelectric

Received: January 22, 2019

Revised: March 31, 2019

Published online: April 24, 2019

- 
- [1] P. Tao, G. Ni, C. Song, W. Shang, J. Wu, J. Zhu, G. Chen, T. Deng, *Nat. Energy* **2018**, *3*, 1031.
- [2] M. Gao, L. Zhu, C. K. N. Peh, G. W. Ho, *Energy Environ. Sci.* **2019**, *12*, 841.
- [3] L. Zhu, M. Gao, C. K. N. Peh, G. W. Ho, *Mater. Horiz.* **2018**, *5*, 323.
- [4] L. Zhu, M. Gao, C. K. N. Peh, G. W. Ho, *Nano Energy* **2019**, *57*, 507.
- [5] X. Li, X. Min, J. Li, N. Xu, P. Zhu, B. Zhu, S. Zhu, J. Zhu, *Joule* **2018**, *2*, 2477.
- [6] X.-Q. Wang, C. F. Tan, K. H. Chan, X. Lu, L. Zhu, S.-W. Kim, G. W. Ho, *Nat. Commun.* **2018**, *9*, 3438.
- [7] M.-Q. Yang, M. Gao, M. Hong, G. W. Ho, *Adv. Mater.* **2018**, *30*, 1802894.
- [8] G. Ni, G. Li, S. V. Boriskina, H. Li, W. Yang, T. Zhang, G. Chen, *Nat. Energy* **2016**, *1*, 16126.
- [9] W. Shang, T. Deng, *Nat. Energy* **2016**, *1*, 16133.
- [10] F. Zhao, X. Zhou, Y. Shi, X. Qian, M. Alexander, X. Zhao, S. Mendez, R. Yang, L. Qu, G. Yu, *Nat. Nanotechnol.* **2018**, *13*, 489.
- [11] L. Zhou, Y. Tan, J. Wang, W. Xu, Y. Yuan, W. Cai, S. Zhu, J. Zhu, *Nat. Photonics* **2016**, *10*, 393.
- [12] P. Zhang, J. Li, L. Lv, Y. Zhao, L. Qu, *ACS Nano* **2017**, *11*, 5087.
- [13] T. Li, H. Liu, X. Zhao, G. Chen, J. Dai, G. Pastel, C. Jia, C. Chen, E. Hitz, D. Siddhartha, R. Yang, L. Hu, *Adv. Funct. Mater.* **2018**, *28*, 1707134.
- [14] N. Xu, X. Hu, W. Xu, X. Li, L. Zhou, S. Zhu, J. Zhu, *Adv. Mater.* **2017**, *29*, 1606762.
- [15] G. Ni, S. H. Zandavi, S. M. Javid, S. V. Boriskina, T. A. Cooper, G. Chen, *Energy Environ. Sci.* **2018**, *11*, 1510.
- [16] C. Song, T. Li, W. Guo, Y. Gao, C. Yang, Q. Zhang, D. An, W. Huang, M. Yan, C. Guo, *New J. Chem.* **2018**, *42*, 3175.
- [17] M. Ye, J. Jia, Z. Wu, C. Qian, R. Chen, P. G. O'Brien, W. Sun, Y. Dong, G. A. Ozin, *Adv. Energy Mater.* **2017**, *7*, 1601811.
- [18] Y. Zeng, J. Yao, B. A. Horri, K. Wang, Y. Wu, D. Li, H. Wang, *Energy Environ. Sci.* **2011**, *4*, 4074.
- [19] M. Gao, P. K. N. Connor, G. W. Ho, *Energy Environ. Sci.* **2016**, *9*, 3151.
- [20] K. Bae, G. Kang, S. K. Cho, W. Park, K. Kim, W. J. Padilla, *Nat. Commun.* **2015**, *6*, 10103.
- [21] L. Zhou, Y. Tan, D. Ji, B. Zhu, P. Zhang, J. Xu, Q. Gan, Z. Yu, J. Zhu, *Sci. Adv.* **2016**, *2*, e1501227.
- [22] Y. Wang, L. Zhang, P. Wang, *ACS Sustainable Chem. Eng.* **2016**, *4*, 1223.
- [23] K.-K. Liu, Q. Jiang, S. Tadepalli, R. Raliya, P. Biswas, R. R. Naik, S. Singamaneni, *ACS Appl. Mater. Interfaces* **2017**, *9*, 7675.
- [24] J. Zhou, Z. Sun, M. Chen, J. Wang, W. Qiao, D. Long, L. Ling, *Adv. Funct. Mater.* **2016**, *26*, 5368.
- [25] L. Zhu, M. Gao, C. K. N. Peh, X. Wang, G. W. Ho, *Adv. Energy Mater.* **2018**, *8*, 1702149.
- [26] X. Li, J. Li, J. Lu, N. Xu, C. Chen, X. Min, B. Zhu, H. Li, L. Zhou, S. Zhu, T. Zhang, J. Zhu, *Joule* **2018**, *2*, 1331.
- [27] H. Song, Y. Liu, Z. Liu, M. H. Singer, C. Li, A. R. Cheney, D. Ji, L. Zhou, N. Zhang, X. Zeng, Z. Bei, Z. Yu, S. Jiang, Q. Gan, *Adv. Sci.* **2018**, *5*, 1800222.
- [28] Y. Shi, R. Li, Y. Jin, S. Zhuo, L. Shi, J. Chang, S. Hong, K.-C. Ng, P. Wang, *Joule* **2018**, *2*, 1171.
- [29] M. Zhu, Y. Li, F. Chen, X. Zhu, J. Dai, Y. Li, Z. Yang, X. Yan, J. Song, Y. Wang, E. Hitz, W. Luo, M. Lu, B. Yang, L. Hu, *Adv. Energy Mater.* **2018**, *8*, 1701028.
- [30] X. Li, R. Lin, G. Ni, N. Xu, X. Hu, B. Zhu, G. Lv, J. Li, S. Zhu, J. Zhu, *Nat. Sci. Rev.* **2018**, *5*, 70.
- [31] Z. Liu, H. Song, D. Ji, C. Li, A. Cheney, Y. Liu, N. Zhang, X. Zeng, B. Chen, J. Gao, Y. Li, X. Liu, D. Aga, S. Jiang, Z. Yu, Q. Gan, *Global Challenges* **2017**, *1*, 1600003.
- [32] P.-F. Liu, L. Miao, Z. Deng, J. Zhou, H. Su, L. Sun, S. Tanemura, W. Cao, F. Jiang, L.-D. Zhao, *Mater. Today Energy* **2018**, *8*, 166.
- [33] P. Zhang, Q. Liao, T. Zhang, H. Cheng, Y. Huang, C. Yang, C. Li, L. Jiang, L. Qu, *Nano Energy* **2018**, *46*, 415.
- [34] W. Li, M. C. Tekell, Y. Huang, K. Bertelsmann, M. Lau, D. Fan, *Adv. Energy Mater.* **2018**, *8*, 1802108.
- [35] T. Ding, L. Zhu, X.-Q. Wang, K. H. Chan, X. Lu, Y. Cheng, G. W. Ho, *Adv. Energy Mater.* **2018**, *8*, 1802397.
- [36] W. Liu, Z. Chen, G. Zhou, Y. Sun, H. R. Lee, C. Liu, H. Yao, Z. Bao, Y. Cui, *Adv. Mater.* **2016**, *28*, 3578.
- [37] H. Li, Y. Ding, H. Ha, Y. Shi, L. Peng, X. Zhang, C. J. Ellison, G. Yu, *Adv. Mater.* **2017**, *29*, 1700898.
- [38] Y. Song, H. Chen, Z. Su, X. Chen, L. Miao, J. Zhang, X. Cheng, H. Zhang, *Small* **2017**, *13*, 1702091.
- [39] S.-J. Choi, T.-H. Kwon, H. Im, D.-I. Moon, D. J. Baek, M.-L. Seol, J. P. Duarte, Y.-K. Choi, *ACS Appl. Mater. Interfaces* **2011**, *3*, 4552.
- [40] J. Hong, J. Lee, C. K. Hong, S. E. Shim, *Curr. Appl. Phys.* **2010**, *10*, 359.
- [41] S. Y. Kwon, I. M. Kwon, Y.-G. Kim, S. Lee, Y.-S. Seo, *Carbon* **2013**, *55*, 285.
- [42] Z.-Z. Luo, S. Hao, X. Zhang, X. Hua, S. Cai, G. Tan, T. P. Bailey, R. Ma, C. Uher, C. Wolverton, V. P. Dravid, Q. Yan, M. G. Kanatzidis, *Energy Environ. Sci.* **2018**, *11*, 3220.
- [43] J. L. Blackburn, A. J. Ferguson, C. Cho, J. C. Grunlan, *Adv. Mater.* **2018**, *30*, 1704386.
- [44] H. Zhu, R. He, J. Mao, Q. Zhu, C. Li, J. Sun, W. Ren, Y. Wang, Z. Liu, Z. Tang, A. Sotnikov, Z. Wang, D. Broido, D. J. Singh, G. Chen, K. Nielsch, Z. Ren, *Nat. Commun.* **2018**, *9*, 2497.